Applied Catalysis A, General xxx (xxxx) 118751

Contents lists available at ScienceDirect

Applied Catalysis A, General

journal homepage: www.elsevier.com/locate/apcata

Insights into catalyst structure, kinetics and reaction mechanism during propane dehydrogenation on Pt-Ge bimetallic catalysts

Sajjad Rimaz [a, b], Mohammadreza Kosari [a, b], Luwei Chen [a], Shibo Xi [a], Antonio Monzón [c], Sibudjing Kawi [b, *], Armando Borgna [a, *]

[a] Institute of Sustainability for Chemicals, Energy and Environment (ISCE2), Agency for Science, Technology, and Research, 1 Pesek Road, Jurong Island, 627833, Singapore
[b] Department of Chemical and Biomolecular Engineering, National University of Singapore, 4 Engineering Drive 4, 117585, Singapore
[c] Department of Chemical and Environmental Engineering, Institute of Nanoscience and Materials of Aragón (INMA), CSIC-University of Zaragoza, Spain

ARTICLE INFO

Keywords:
Dehydrogenation
Pt catalysts
Bimetallic Pt-Ge
Kinetics
Alloy
Ensemble
Propylene

ABSTRACT

In the present work, in-depth characterization techniques combined with kinetic analyses were used to develop a deep understanding of the remarkable catalytic performance observed during propane dehydrogenation (PDH) over Ge-promoted Pt/SiO_2. Following our previous work on Pt-Ge/Al_2O_3, we found Ge to significantly affect Pt catalytic performance, reaction mechanism and kinetics, regardless of the nature of the support. The synthesized catalysts were characterized using XAS, XPS, TPR, TGA, C_3H_6/C_3H_8-TPD, HRTEM, CO-chemisorption, BET, and CO-DRIFT. Upon Ge promotion to Pt nanoparticles supported on a large, neutral, SiO_2 surface area, the bimetallic samples showed higher activation energy, lower desorption energy of C_3H_6, lower coke formation rates, and higher C_3H_6 selectivity as compared to the results from using the unpromoted catalyst. Ruling out the neutral SiO_2's support effect, the kinetic study indicates the C_3H_8 reaction order remains close to 1 for all the samples, while the H_2 reaction order decreases from 0.04 to − 0.52 with increasing Ge loading from 0 wt% to 5 wt%. According to the kinetic analysis, the first C-H bond cleavage seems to be the rate-determining step. The addition of Ge enhances the adsorption of hydrogen, which explains the change of the hydrogen reaction order and the apparent activation energy exhibited by the bimetallic samples.

1. Introduction

Due to the widespread applications of propylene derivatives, there is an increasing gap between the supply and demand of propylene [1–4]. The most efficient technology for producing propylene to fill this gap, among all available options, is direct propane dehydrogenation (PDH) reaction [5,6]. The PDH reaction is an endothermic, equilibrium-limited reaction commonly carried out with CrO_x or Pt as base catalysts [7,8]. However, the CrO_x catalyst suffers from severe deactivation due to the large amount of carbon deposition and must be frequently regenerated when used in the PDH reaction [9]. This regeneration step usually results in CrO_x being incorporated into the Al_2O_3 matrix, resulting in the loss of active sites [10]. Additionally, CrO_x catalysts cause environmental concerns, which limits their large-scale application. Supported Pt catalysts are more active in the PDH reaction than CrO_x catalysts are; however, supported Pt catalysts are susceptible to the strong interaction between Pt and C_3H_6, which causes deep dehydrogenation, hydrogenolysis, accelerated coke formation, and, as a result, rapid catalyst deactivation [11–14]. Promoters such as Sn, Cu, Ga, etc. are commonly used to weaken the interaction between Pt and propylene without affecting the Pt-C_3H_8 interaction [10,15,16]. These promotors can suppress side reactions, minimize sintering of Pt nanoparticles, and accelerate the diffusion of coke species from Pt to the support. It is worth mentioning that pure Pt clusters possess a high number of isomers and unpaired electrons with very high activity toward C-C bond cleavage. Promotors such as Si quench spins and cause Pt clusters to become more globular with fewer valence-unsaturated sites, resulting in better activity toward C-H bond activation and lower activity for C-C bond cleavage, which improves selectivity [17].

Catalytic performance and catalyst deactivation using different promotors have been widely investigated for the PDH reaction. For example, recent research on the modification of Pt properties for the PDH reaction have documented the use of Bi, Mn, Sb, Co, and In, among others [18–22]. Concurrently, various characterization techniques have been

* *
* *
E-mail addresses: chekawis@nus.edu.sg (S. Kawi), armando_borgna@ices.a-star.edu.sg (A. Borgna).

https://doi.org/10.1016/j.apcata.2022.118751
Received 31 August 2021; Received in revised form 17 June 2022; Accepted 22 June 2022
0926-860/© 20XX

Note: Low-resolution images were used to create this PDF. The original images will be used in the final composition.

used to clarify the interaction between Pt and the promoters, with the possibility of modulating both geometric and electronic properties of Pt-based catalysts by synthesizing intermetallic compounds and alloys with different structures being highlighted [21]. The excellent propylene selectivity (> 99 %) on these intermetallic structures originates from the geometric effect, which minimizes side reactions such as hydrogenolysis [20]. This different catalytic performance could be attributed to the variation in the adsorption heat of the reactants. Thus, the hydrocarbon and hydrogen's lower adsorption heat results in higher selectivity to propylene. Despite the high number of outstanding studies in this ambit, many fewer efforts have been devoted to investigating the kinetics and reaction mechanism of these novel and modified catalysts in the PDH reaction.

In most of the reported kinetic data for propane dehydrogenation, the reaction order with respect to H_2 varies from − 2–1, while the propane reaction order remains close to 1 [23,24]. A detailed kinetic model has been previously developed for different sizes of monometallic Pt nanoparticles supported on a hydrotalcite-type support to correlate the variation in the hydrogen reaction order with the varying particle size [25]. It was reported that increasing Pt particle size leads to a decrease in activity, resulting in a change in the reaction order with respect to hydrogen and a different reaction mechanism [25]. The addition of promoters could also decrease the activity of Pt nanoparticles and might have a similar effect on reaction order to the one observed when increasing particle size [26,27]. However, understanding of the effect of promotors on the hydrogen and propane reaction order on bimetallic Pt-based catalysts is still lacking.

We have previously demonstrated the positive effect of Ge on enhancing propene selectivity and depressing coke formation in the PDH reaction via the novel Pt-Ge/Al_2O_3, CaO-modified Pt-Ge/Al_2O_3, and Pd-Ge/SiO_2 [26,28,29]. Nevertheless, the kinetics of the Pt-Ge catalysts in the PDH reaction, especially the effect of alloy formation on the reaction orders with respect to hydrogen and propane, remains to be understood. Accordingly, in the present contribution (Scheme 1), a detailed kinetic study is reported on Pt nanoparticles modified with GeO_x supported on a high-surface-area SiO_2 as a neutral support, in which study the kinetic parameters are correlated with the catalyst structure. To rule out the support effect, a neutral SiO_2 support with a high surface area has been selected to thwart the effect of acidic sites on catalytic performance and catalyst deactivation, permitting a more accurate understanding of the impact of Ge/GeO_x on the catalyst structure and on the reaction mechanism and kinetics.

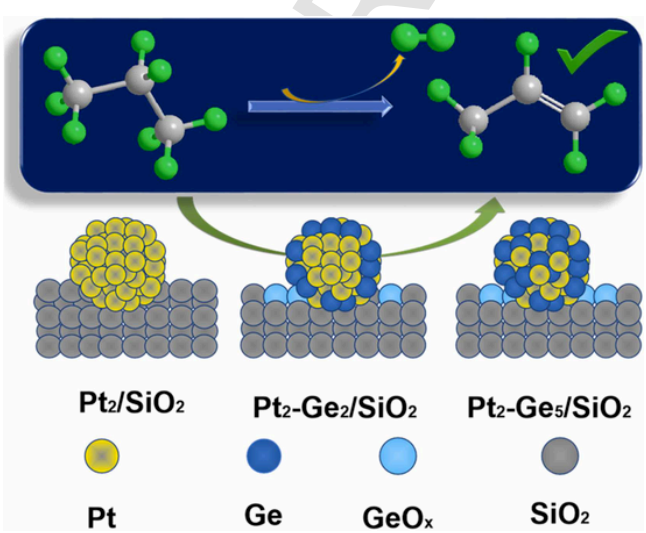

Scheme 1. Illustration of the Ge effect on Pt-based catalysts supported on a neutral and high-surface-area SiO_2 support for the PDH reaction on the impact of alloy formation on the reaction mechanism and kinetics.

2. Experimental

2.1. Catalyst preparation

The bimetallic samples, denoted as Pt_2-Ge_x/SiO_2, were prepared via the sequential incipient wetness impregnation (IWI) method using [Pt $(NH_3)_4$] $(NO_3)_2$ and $GeCl_4$ (Alfa Aesar, > 99.9 %) as precursors. All the samples had 2 wt % Pt, while the Ge loading was between 0 wt% and 8 wt%. SiO_2 (Silica Gel 60, KANTO CHEMICAL CO, 751 m^2/g and 1.2 ml/g pore volume) was used as the support. The support was first calcined at 700 °C for 2 h before synthesizing the catalysts. For the catalyst synthesis, $GeCl_4$ was initially dissolved in ethanol and added dropwise to the support. Then the sample was dried at 120 °C overnight and calcined at 250 °C for 3 h. The impregnating of Pt was carried out by dissolving [Pt $(NH_3)_4$] $(NO_3)_2$ in water, and NH_3 was added to ensure a pH of 11. Finally, the prepared samples were dried at 120 °C overnight and calcined at 250 °C for 3 h with a heating rate of 5 °C/min. Prior to the reaction and characterization, the catalysts were reduced at 300 °C for 0.5 h and 600 °C for 1 h with flowing 40% H_2/N_2 (50 ml/min).

2.2. Catalyst characterization

A Micromeritics ASAP 2420 apparatus was used to measure the Brunauer-Emmett-Teller (BET) specific surface areas of the catalysts. The reduced samples were pretreated at 200 °C overnight under vacuum prior to performing the isotherms at 77 K. Pore volumes were obtained using the Barrett-Joyner-Halenda (BJH) method.

Morphology, particle size and chemical composition of the nanoparticles were investigated using high-resolution TEM with energy-dispersive X-ray spectroscopy (HRTEM/EDX, JEM-2100 F).

Dispersion and the metallic surface area of the samples were measured by CO-chemisorption using a Micromeritics ASAP 2020 automated adsorption analyser. Around 50 mg catalyst was reduced in situ as indicated in Section 2.1. After evacuation at 350 °C, samples were cooled down to room temperature for analysis. The CO stoichiometry to Pt was 1:1, and actual loading of Pt obtained from ICP-OES was used for the analysis.

An inductively coupled plasma optical emission spectrometer (ICP-OES) was used to obtain the actual loading of Pt in the samples. Before the measurements, 100 mg of catalyst was dissolved in a solution of sulfuric and phosphoric acids assisted by microwave digestion, then diluted 400 times with water.

The desorption energy of the propylene was measured using a TPD system equipped with a mass spectrometer (Hiden). A sample amount of 50 mg was loaded in a quartz tube held by quartz wool. Prior to analysis, the catalysts were reduced as described above. After reduction, the sample was cooled in flowing N_2 to room temperature (RT) and purged for 1 h. Then it was saturated with C_3H_6 (5 % in N_2, total flow rate: 50 ml/min) for 0.5 h. After saturation, the sample was again purged with nitrogen (20 ml/min, 0.5 h). The temperature was ramped up from RT to 500 °C at different ramping rates (2 °C/min, 5 °C/min, 8 °C/min, and 11 °C/min), and C_3H_6 desorption profiles were determined with a mass spectrometer. The following formula was used in the calculations [11,30]:

$$Ln\left(\frac{\beta}{T_p{}^2}\right) = -\frac{E_d}{R \times T_p} + \ln\left(\frac{E_d \times A}{R \times C}\right) \quad (1)$$

where β is the ramp rate (K/min), T_p is the desorption temperature (K), E_d is the desorption energy (kJ/mol), A is the total adsorbed gas at saturation state (cm^3/g), R is the specific gas constant (kJ/(mol.K)), and C is a constant.

Temperature programmed reduction (TPR) profiles were measured using a TPDRO 1100 system (Thermo Scientific) equipped with a TCD detector. Before each analysis, around 100 mg of catalyst was outgassed

in Ar at 150 °C for 1 h then allowed to cool to room temperature. The measurements were carried out using a 5 % H_2/95 % Ar mixture (50 ml/min), while temperature was ramped up from 50 °C to 950 °C.

An FT-IR spectrometer (Frontier, PerkinElmer) equipped with a mercury-cadmium-telluride (MCT) detector was used to perform a diffuse reflectance infrared Fourier transform spectroscopy (DRIFTS) analysis. The catalyst was placed in a drift cell fitted with ZnSe windows and was reduced in situ. Temperature was cooled to 30 °C under He. Then the catalyst was saturated with 2 % CO/He (50 ml/min) for 0.5 h, and physically adsorbed CO was removed before the spectra were taken under He.

X-ray photoelectron spectroscopy (XPS) was performed using a VG ESCALAB 250 instrument with an excitation source of Mg K_α radiation. Catalysts were reduced *ex situ* as previously indicated. After reduction, samples were moved to a glovebox without contacting with air and loaded in the XPS holder. With the protection of an inert gas, the holder was moved to the XPS chamber and eveacuated for 2 h for removing surface species. The spot size was 300 μm × 100 μm. To minimize the beam-induced reduction of metal species, the beam was moved to a new spot on the sample powder (vide infra) for each measurement. XPS spectra were obtained in the normal emission geometry with a pass energy of 20 eV and a step size of 0.1 eV for C 1 s and 0.05 eV for Pt4f. Between 5 and 8 scans were recorded for each core level, and the duration of the spectrum acquisition for each core level was almost 5 min. The binding energies were corrected, and the spectra were normalized before applying a Shirley background. XPSPEAk41 software was used to perform least-square fittings using Gaussian-Lorentzian profiles for spectra deconvolution. The best optimization parameters were derived using the following constraints: (1) a spin-orbit splitting of 3.35 eV for Pt 4 f7/2 and 4 f5/2, (2) an area ratio of 4:3 for Pt 4 f 7/2: Pt 4 f 5/2, and (3) an equal Gaussian-Lorentzian ratio for Pt 4f7/2 and Pt 4f5/2.

A value of 284.8 eV for C 1 s peak position was used as an internal standard for the correction of binding energies.

In-situ X-ray absorption spectra (XAS) were performed at the XAFCA beamline at the Singapore Synchrotron Light Source [31]. After the sample wafers were reduced in situ under 40 %H_2 in He (50 ml/min), the temperature was decreased to RT under He, and the spectra were collected. WinXAS software was used for data analysis.

TGA analysis was used to study carbon deposition on the spent samples. Each sample was heated from 30 °C to 900 °C with a ramping rate of 5 °C/min under a 40:60 air/N_2 mixture.

2.3. Catalytic test

The PDH reaction was performed in a fixed-bed quartz tube reactor (5 mm ID, 600 mm length). A 50 mg amount of the sample diluted with SiC was loaded into the reactor and held by quartz wool. Prior to the reaction, the catalysts were reduced using the same protocol described before. After reduction, the catalyst was purged with N_2 for 0.5 h and cooled to the reaction temperature. The reaction temperature was varied between 450 °C and 525 °C at a pressure of 1 atm. After temperature stabilization, feed was introduced into the reactor at a flow rate of 80 ml/min. C_3H_8 and H_2 partial pressures of the feed was varied between 2 kPa and 12 kPa using an N_2 balance. Argon was used as the internal standard for calculating the outlet flow rate. Analysis of the products was performed by an online 2014 Shimadzu GC equipped with an FID detector for hydrocarbon detection (Column: GS-GASPRO 30 m length, 32 mm ID) and a TCD detector for detecting hydrogen (Column: HayeSep D). The evaluation of the catalytic performance was performed using the following equations:

$$\text{Propane Conversion } (X_P)\ (\%) = \frac{(F_{Propane})_{in} - (F_{Propane})_{out}}{(F_{Propane})_{in}} \cdot 100 \quad (2)$$

$$\text{Product Selectivity } (S_i)\ (\%) = \frac{\left(\frac{n_i}{3}\right) \cdot (F_i)_{out}}{\sum_i \left(\frac{n_i}{3}\right) \cdot (F_i)_{out}} \cdot 100 \quad (3)$$

$$\text{Propane rate } (\text{mol}/(g_{Pt} \cdot s)) = \frac{\frac{F_{C_3H_8}}{22400 \times 60}}{m_{cat} \times w_{Pt}} \cdot X_p \quad (4)$$

$$\text{TOF } (1/S) = \frac{\frac{F_{C_3H_8}}{22400 \times 60}}{m_{cat} \times w_{Pt} \times D_{Pt}} \cdot X \cdot 195.084 \quad (5)$$

In these equations, F_i, n_i, t, X_{in}, X_{end}, m_{cat}, and w_{pt} are hydrocarbon flow rate (ml/min), number of carbon atoms, reaction time (h), initial conversion, conversion at end of reaction, loading of catalyst (g), and percentage of Pt, respectively.

3. Results and discussion

3.1. Morphological and physicochemical characterization

Illustrated in Fig. 1(a), the HRTEM images of the as-synthesized samples (in reduced form) demonstrate the formation of fine metal nanoparticles on monometallic Pt_2/SiO_2 and bimetallic PtGe in Pt_2-Ge_2/SiO_2, Pt_2-Ge_5/SiO_2, and Pt_2-Ge_8/SiO_2 catalysts, with particle sizes of 3.3 ± 0.7, 3.5 ± 0.4, 3.7 ± 0.9, and 3.9 ± 0.9 nm, respectively. Expectedly, as Ge is added to the samples, the particle size is increased slightly but certainly remains within the range of 3–4 nm, with an average of 3.6 nm. Concerning the alloy formation in bimetallic samples, for example, the captured lattice fringes inserted in Fig. 1(a) and (d) of monometallic Pt_2/SiO_2 and bimetallic Pt_2-Ge_2/SiO_2 obviously exhibit an elongated nanoparticle for the latter compared to the monometallic sample, where Pt particles with a regular shape are clearly observable. Such an elongated nanoparticle for the latter bimetallic Pt_2-Ge_2/SiO_2 might indicate alloy formation, resulting in dilution of the Pt surface. To confirm this, an HRTEM/EDX pattern of each sample was also captured. Firstly, the HRTEM/EDX elemental mappings of the monometallic and bimetallic samples exhibit an even distribution of Pt and Ge over the SiO_2 surface, with no localized aggregation of these elements (Fig. 1 (b), (e), (h) and (k)). Secondly, the HRTEM-EDX line-scan patterns of individual particles, shown in Fig. 1(c), (f), (i) and (l), confirm that both Pt and Ge are present in the nanoparticles, which might indicate surface dilution or alloy formation. As seen in the line-scan patterns, the Ge signal (shown by a red line) over the Pt surface (shown by a cyan line) starts to appear as Ge is added to the samples. Moreover, the Ge signal intensifies as the Ge concentration is increased in the bimetallic samples. Based on these patterns, it might be reasonable to expect that some Ge is present beneath the Pt atoms, forming a subsurface-regulated PtGe nanoparticle, similar to the case of PtGa reported elsewhere [32].

The textural properties of the samples, measured by N_2 physisorption, are reported in Table 1 and Fig. S1. The BET surface area and total pore volume of the support material (SiO_2) after calcination were 498 m^2/g and 0.79 cm^3/g, respectively. After loading of Pt and Ge onto the support, the BET surface area decreased. Alvarez-Galvan et al. reported a similar observation after metal loading on the catalyst support [33]. Long et al. also reported the blockage of support channels by the impregnated metals, reducing the BET surface area [34]. Accordingly, the decrease in the BET surface area of the samples was most probably due to pore or channel blockage by the metal particles. It is also worthy to stress that the co-addition of Pt and Ge results in only a slight change in the BET surface are, showing a decreasing trend similar to what has been previously reported for other supports [26].

Metal dispersion and metallic surface area were measured with CO-chemisorption, and the results are presented in Table 1. As shown in this table, metal dispersion and metal surface area of the samples exhibited a decreasing trend with increasing Ge loading. As it is well demon-

UNCORRECTED PROOF

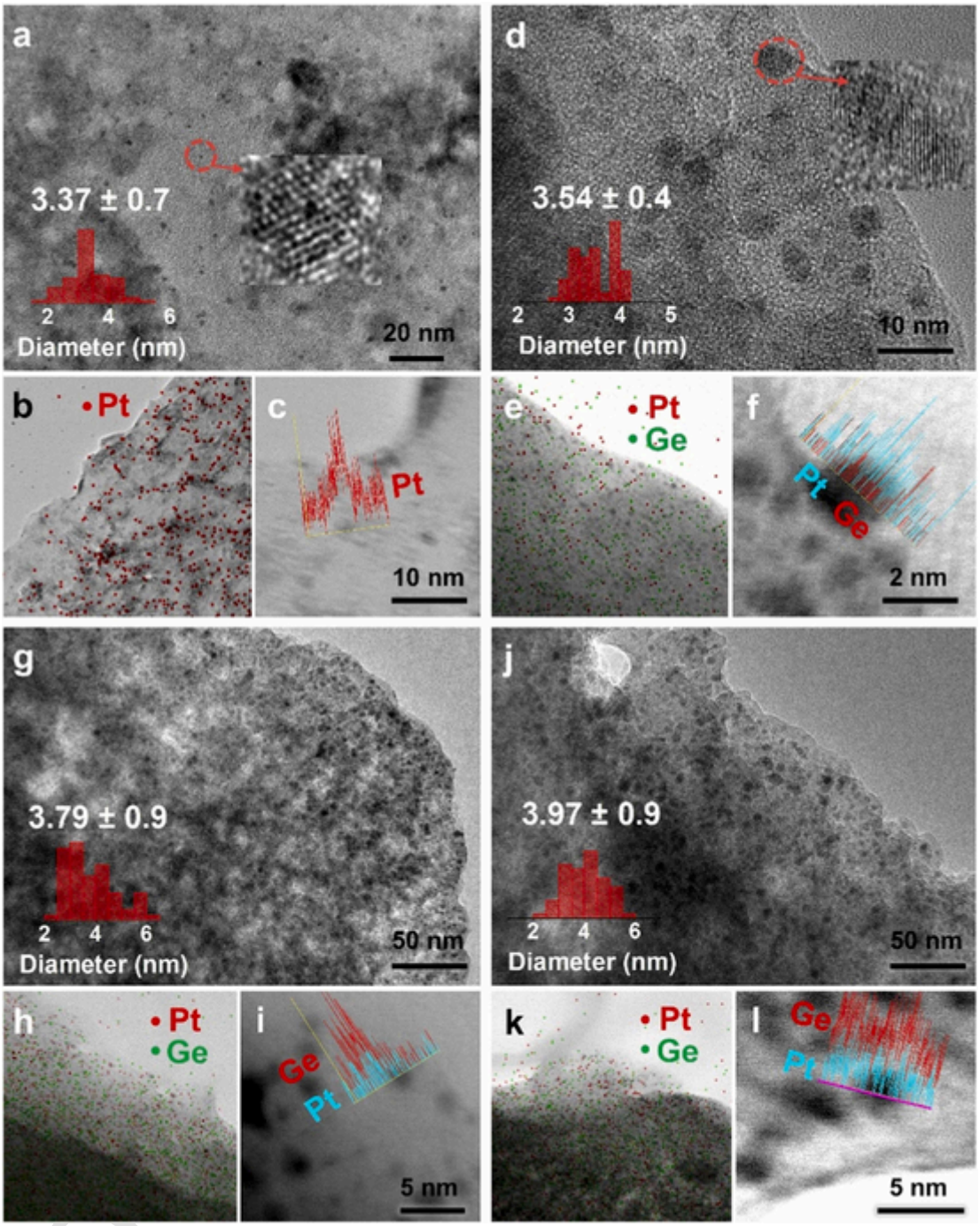

Fig. 1. HRTEM images and corresponding particle-size distribution of (a) Pt_2/SiO_2, (d) Pt_2-Ge_2/SiO_2, (g) Pt_2-Ge_5/SiO_2, and (j) Pt_2-Ge_8/SiO_2 samples in reduced form. HRTEM-EDX (b, e, h and k) elemental mappings of a large sample area and (c, f, i and l) line scans of an individual particle of corresponding samples shown in (a) Pt_2/SiO_2, (d) Pt_2-Ge_2/SiO_2, (g) Pt_2-Ge_5/SiO_2, and (j) Pt_2-Ge_8/SiO_2. Note: inserted pictures in figures (a) and (b) are higher magnifications of a single nanoparticle.

strated, partial coverage of the Pt surface upon adding a second metal is the main reason for the decrease of both dispersion and surface area of Pt [26,35]. Accordingly, Ge partially blocks and covers Pt's metallic surfaces, resulting in a lower dispersion and metallic surface area. These changes in Pt's dispersion and metallic surface area clearly indicate the existence of an interaction between Pt and Ge, which will be investigated thoroughly in the next sections.

3.2. *Understanding electronic and structural properties of Pt-Ge bimetallic catalysts supported on SiO_2*

In-situ infrared spectroscopy of adsorbed carbon monoxide (CO) is a valuable technique for studying the interaction between metals to unravel their modified geometric and electronic properties as compared to their pristine counterparts. Accordingly, CO-DRIFT was used to study electronic and geometric properties of the catalysts, and the results are depicted in Fig. 2. For the Pt catalysts, the vibration band of bridge-bonded CO appears between 1750 cm^{-1} and 1900 cm^{-1}, while the linearly bonded CO vibration band appears between 1900 cm^{-1} and 2200 cm^{-1} [36]. The spectrum of the monometallic Pt sample shows

Table 1
Physiochemical properties of the catalysts.

Sample	Pt loading (ICP)	V_{total} (cm^3/g)	BET surface area (m^2/g)	BJH pore size (nm)	Metal Dispersion (%)	Metal surface area (m^2/g_{cat})
SiO_2	–	0.79	498	3.0	–	–
Pt_2/SiO_2	2.01	0.72	457.9	3.1	41.8	2.06
Pt_2-Ge_2/SiO_2	1.95	0.79	477.4	3.3	22.1	1.2
Pt_2-Ge_5/SiO_2	2.10	0.76	447.3	3.3	12.5	0.6
Pt_2-Ge_8/SiO_2	1.96	0.74	441.2	3.2	10.4	0.5

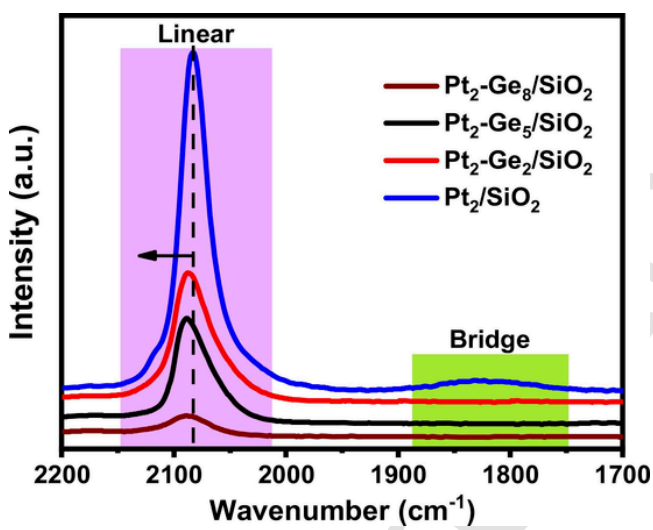

Fig. 2. CO-DRIFT spectra of the samples with different Ge loadings.

the presence of both bands, while the bridge-bonded CO has completely disappeared upon Ge addition. This agrees well with the literature, which ascribes the disappearance of bridge-bonded CO on the surface of Pt upon adding a second metal to the surface dilution of Pt and the breakage of the Pt ensembles [16]. Furthermore, after introducing Ge onto the support, the intensity of linearly bonded CO decreases and shifts to a higher wavenumber. In bimetallic Pt-based catalysts, when electrons are transferred from Pt to the second metal, the electron transfer from Pt to the antibonding 2π orbitals of adsorbed CO is diminished, resulting in a decrease in the strength of the C-O bond and, therefore, an increase in C-O frequency [26,37]. Accordingly, after adding Ge to the samples, Pt becomes electron-deficient as pointed out by a redshift in the spectra of the bimetallic samples. Such a shift in the CO-DRIFT spectra of the Ge-modified samples indicates the existence of a close interaction between Pt and Ge, which can be due to bulk and/or surface alloy formation, resulting in a modification of geometric and electronic properties [16]. This interaction will be further elaborated in the following sections.

XPS analysis was used to investigate the chemical state and electronic properties of Pt and Ge. For Pt, as is well known, the most intense photo-emission line in the XPS spectra corresponds with the Pt 4 f core level. Accordingly, the Pt 4 f XPS spectra of the samples were measured, and the results are depicted in Fig. 3. Obviously, upon introducing Ge to Pt, the binding energy has shifted to a higher value. For monometallic

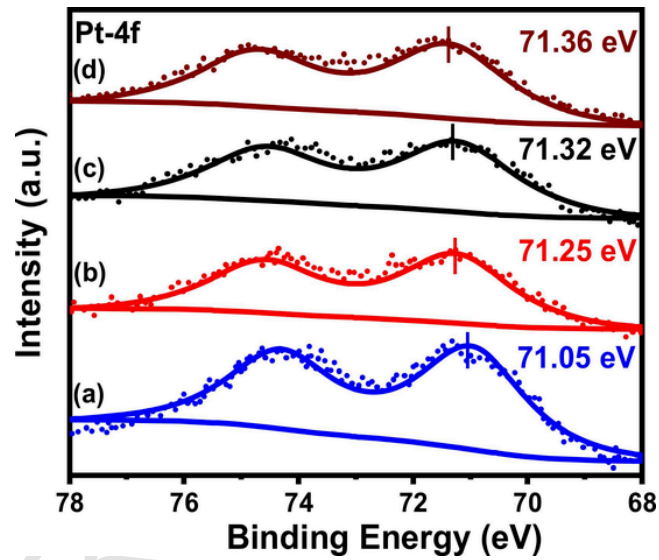

Fig. 3. Pt 4 f XPS spectra of the samples: (a) Pt_2/SiO_2, (b) Pt_2-Ge_2/SiO_2, (c) Pt_2-Ge_5/SiO_2, (d) Pt_2-Ge_8/SiO_2.

Pt_2/SiO_2, the Pt 4 f binding energy is 71.04 eV, similar to the reported BE for metallic Pt [16]. With adding 2 wt%, 5 wt% and 8 wt% Ge, the binding energies have been shifted to 71.25 eV, 71.32 eV, and 71.36 eV, respectively. Ren et al. reported that upon gold being added to Pt, electrons were transferred from Pt to Au due to the alloy formation, and as a result, the Pt 4 f XPS spectra shifted to higher binding energies [16]. Our results also indicate an electronic modification of Pt upon the addition of Ge, which can be ascribed to the thermal diffusion of Ge into the Pt structure, forming a Pt-Ge alloy and resulting in the shift of the binding energies to higher values.

XAS measurements of the Pt L_{III} and Ge K edges were carried out to further elucidate alloy formation and the interaction between Pt and Ge in the Pt-Ge catalysts. Pt L_{III} edge X-ray absorption near edge structure (XANES) analysis of the samples is depicted in Fig. 4(a). The Pt_2/SiO_2 white line has the shape and intensity similar to that of the Pt foil, suggesting that Pt atoms have been fully reduced and the environment of the Pt atoms is similar to the one on bulk Pt metal [18]. XANES spectra of Pt_2-Ge_2/SiO_2 and Pt_2-Ge_5/SiO_2 are slightly different compared to Pt_2/SiO_2, showing a noticeable increase in the intensity of the white line and a slight shift to higher energy levels. Ye et al. also observed similar shifts in the XANES spectra after adding Sb to Pt and at an increasing Sb/Pt molar ratio. They correlated observed changes in the XANES spectra to the increased energy level of empty Pt 5d states, intermetallic interaction and alloy formation between Pt and Sb [20]. Accordingly, the changes in the white line intensity and position of the samples depicted in Fig. 4(a) imply alloy formation and electronic effects of Ge on Pt, in line with XPS and CO-DRIFT results. As shown in this figure, in bimetallic Pt-Ge samples, Ge withdraws electrons from neighboring Pt atoms, which is indicated by the increase in the intensity of the white line. Borgna et al. also reported that upon alloy formation between Pt and Ge, Ge increases the electrophilic character of Pt, resulting in an increase in the intensity of the white line [37].

Ge K edge XANES spectra of the samples are presented in Fig. S5. These spectra suggest that Ge bulk remains mostly as an oxide, in good agreement with the TPR profiles (Fig. S4) and XPS results (Figs. S2 and S3) [21]. Recently, a similar behavior has been reported for Sb-Pt bimetallic samples, where XANES spectra of the Sb K edge of the samples with different Sb/Pt ratios remain almost similar to those of the oxide ones [20].

Extended X-ray absorption fine structure (EXAFS) spectra of the Pt L_{III}-edge are shown in Fig. 4(b). Three peaks indicating a typical metallic Pt-Pt scattering were observed in the EXAFS spectrum of the

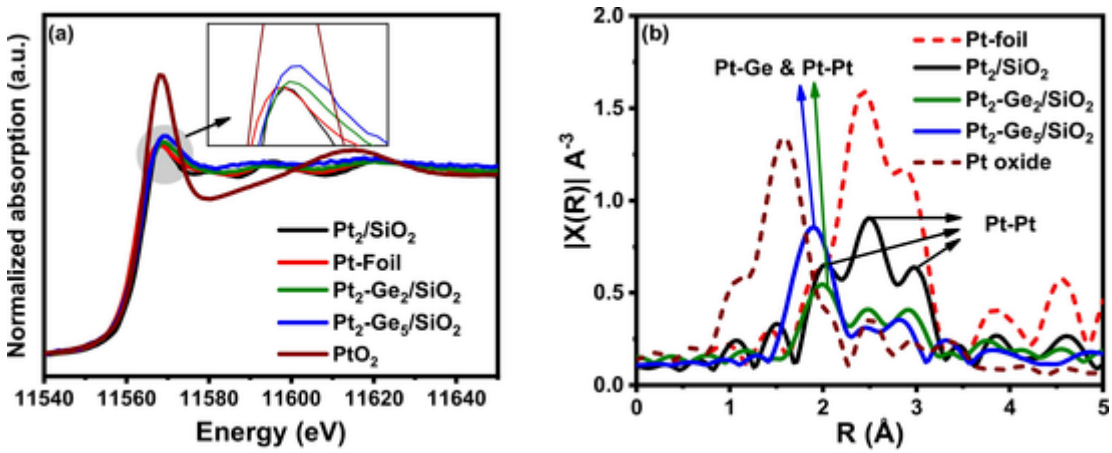

Fig. 4. (a) Pt L_{III} edge X-ray absorption near edge structure (XANES) of the samples; (b) FT of the EXAFS spectra of the reduced samples.

monometallic Pt_2/SiO_2 catalyst [22]. After adding Ge at increasing Ge/Pt ratios, the positions and intensities of the peaks changed significantly. Ye et al. reported that upon introducing other metals to Pt/SiO_2 catalysts, the neighboring Pt atoms are no longer only Pt atoms, resulting in changes of both peak position and relative intensity in the EXAFS spectra [20]. Accordingly, the changes in the EXAFS spectra of Pt after introducing Ge clearly indicate the formation of Pt-Ge bonds.

Table 2 reports the EXAFS parameters, including bond distance (R), coordination number (CN), and Debye Waller factor (σ^2), which were obtained via EXAFS fitting. According to the fitting results, it is obvious that Pt CN decreased as Ge was added to the samples. For example, Pt CN is 8.9 for the Pt-Pt bond in the Pt_2/SiO_2 sample, while it changes to 5.8 and 3.5 for the Pt_2-Ge_2/SiO_2 and Pt_2-Ge_5/SiO_2 samples, respectively. On the other hand, from the EXAFS fitting, Pt-Ge coordinations are clearly detected upon Ge being added to the samples, with CN values of 1.5 and 3.1 for the Pt_2-Ge_2/SiO_2 and Pt_2-Ge_5/SiO_2 samples, respectively. Thus, it is clearly demonstrated that: (i) alloy formation between Pt and Ge readily occurs in both samples, and (ii) the number of Ge neighbor atoms around Pt is higher in Pt_2-Ge_5/SiO_2 compared to Pt_2-Ge_2/SiO_2. However, Pt-Pt and Pt-Ge bond distances remain fairly constant with a slight decrease of the Pt-Ge distance in the sample with the higher Ge loading. Besides, no Pt-O coordinations are found during the fittings, highlighting the full reduction of Pt and successful formation of a metallic alloy.

Finally, it is important to stress that the GeOx species spread out onto the SiO_2 support can be considered as inert in propane dehydrogenation. Hence, GeOx species are expected only to modify the size of the metal particles and/or acid properties of the support. As shown by HRTEM, the size of the metal particles is only marginally increased by GeOx. Since we have previously reported that the addition of GeOx has not led to a noticeable change in both total acidity and strength distribution on Al_2O_3-supported catalysts [28], the modification acid properties can also be safely ruled out.

Table 2
Structural Parameters of Catalytic Samples Obtained via EXAFS Fittings.

No.	Sample	Bond	R (Å)[a]	CN[b]	σ^2 (Å^2)[c]	R-factor
1	Pt_2/SiO_2	Pt-Pt	2.76(0.01)	8.9(1.0)	0.0061(0.0007)	0.012
		Pt-Ge	N.A.	N.A.	N.A.	
2	Pt_2-Ge_2/SiO_2	Pt-Pt	2.75(0.01)	5.8(0.5)	0.0082(0.0006)	0.002
		Pt-Ge	2.42(0.01)	1.5(0.3)	0.0076(0.0015)	
3	Pt_2-Ge_5/SiO_2	Pt-Pt	2.74(0.01)	3.5(0.8)	0.0094(0.0015)	0.001
		Pt-Ge	2.37(0.01)	3.1(0.4)	0.0082(0.0008)	

[a] bond distance in Angstroms.
[b] coordination number.
[c] Debye-Waller factor.

Therefore, changes in the structural and electronic properties of Pt atoms strongly modifies the interaction of Pt with the reactants and products during the PDH reaction, thus significantly affecting the catalytic performance. Since the desired product from the PDH reaction is propylene, the effect of Pt-Ge alloying on the interaction between Pt and propylene needs to be clarified. This interaction will be discussed in detail in the next section.

3.3. Ge effect on propylene adsorption

C_3H_6-TPD was employed to investigate the interaction between C_3H_6 (the desired product from the PDH reaction) and Pt and to estimate the desorption energy of C_3H_6 for Pt and the Pt-Ge samples. For this purpose, desorption profiles of the samples were recorded with different heating rates. For example, the TPD profiles obtained with a 2 °C/min rate are depicted in Fig. 5(a), (profiles for the other heating rates are shown in Fig. S6). Two peaks appeared in the C_3H_6-TPD profiles of the catalysts. The first one, which appeared at a relatively low temperature, is related to weakly adsorbed propylene on the Pt surface. The second peak, desorbing at a higher temperature, corresponds to C_3H_6 being strongly adsorbed on the metal surface. Interestingly, with adding Ge at increasing loadings, propylene's desorption temperature decreases, clearly indicating that Ge weakens the interaction between Pt and C_3H_6, resulting in lower amount of C_3H_6 adsorbed on the Pt surface. The significant decrease in the desorption temperature when the Ge loading increases from 5 wt% to 2 wt% can be ascribed to the higher degree of alloy formation, as clearly revealed by EXAFS analysis.

The C_3H_6-TPD results in combination with Eq. (1) can be used to determine the desorption energy of C_3H_6 from the samples. According to this equation, the slope of $Ln\left(\frac{\beta}{T_P{}^2}\right)$ versus $\frac{1}{T_p}$ plots gives the desorption energy (kJ/mol) of propylene. Fig. 5(b) shows the $Ln\left(\frac{\beta}{T_P{}^2}\right)$ versus $\frac{1}{T_p}$ plot, and the desorption energies have been calculated for samples with 0 wt%, 2 wt%, and 5 wt% Ge loading. Desorption energy for Pt_2/SiO_2 catalyst is 57 ± 4 kJ/mol, while it decreases to 41 ± 3 kJ/mol for Pt_2-Ge_2/SiO_2 and to 32 ± 3 kJ/mol for Pt_2-Ge_5/SiO_2. These results clearly indicate that Ge decreases the strength of the Pt-C_3H_6 bond.

Indeed, if C_3H_6 adsorbs too strongly on the metal surface, it can be involved in side reactions and deep dehydrogenation, resulting in increased coke formation and poor catalytic performance [15]. Thus, a lower desorption energy of propylene is expected to result in a better catalytic performance and anti-coking effect in the Ge-promoted samples. Moreover, the C_3H_8-TPD profiles (Fig. S7) indicate that propane also adsorbs strongly on the monometallic Pt_2/SiO_2 sample. Strong adsorption of C_3H_8 could be invoked as the reason for the higher conver-

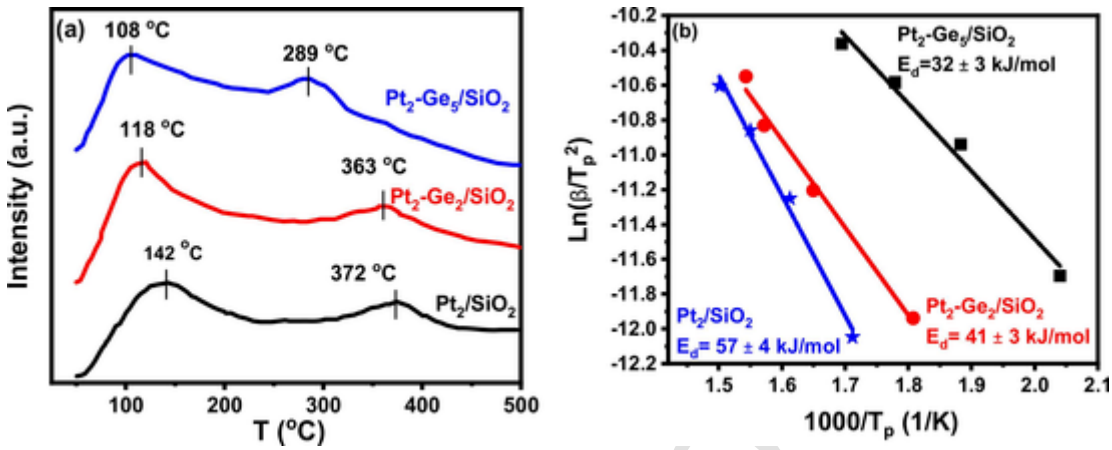

Fig. 5. (a) Propylene TPD profiles of samples (Pt_2/SiO_2, Pt_2-Ge_2/SiO_2, and Pt_2-Ge_5/SiO_2) obtained with a heating rate of 2 °C/min; (b) Propylene desorption energy of the samples derived using different heating rate.

sion of propane on the monometallic sample, especially at the beginning of the reaction [38].

A detailed investigation into the impact of the catalytic performance is presented in the following section.

3.4. Catalytic performance

3.4.1. Effects of Ge loading on catalytic performance

To precisely elucidate the Ge effect on modified Pt catalysts, catalytic performance of the samples with different Ge contents was investigated in the PDH reaction at 798 K. The results of this investigation are shown in Fig. 6. As indicated in this figure, the monometallic Pt_2/SiO_2 sample exhibited a relatively high propane conversion (32.5 %) at the beginning of the reaction. The initial conversion decreased to 27.1 % and 24.9 % upon adding 2 wt % and 5 wt % Ge, respectively. However, selectivity increased from 40.2 % for the monometallic Pt_2/SiO_2 sample to 85.7 % and 97.9 % in Pt_2-Ge_2/SiO_2, and Pt_2-Ge_5/SiO_2, respectively. Obviously, increasing Ge loading resulted in a better stability of the catalyst and an enhancement of propylene selectivity. Moreover, as shown in Fig. S9, the coke formation rate on Pt_2/SiO_2 was 0.50 mg/(g_{cat}·min), while it decreased to 0.365 mg/(g_{cat}·min) for Pt_2-Ge_2/SiO_2, and 0.32 mg/(g_{cat}·min) for Pt_2-Ge_5/SiO_2.

C_3H_6-TPD results previously indicated that increasing Ge loading contributes to a facile desorption of propylene. In fact, it has been reported that facile desorption of C_3H_6 from Pt surfaces decreases the coke formation by preventing deep dehydrogenation of the produced propylene for TiO_2-Al_2O_3-supported and copper-modified Pt catalysts [11,27]. Likewise, a higher selectivity and lower coke formation rate in Ge-modified Pt catalyst are ascribed to the promoting effect of Ge on Pt, which effect causes rapid desorption of C_3H_6 due to the alloy formation, inhibiting its participation in side reactions [26]. It should also be highlighted that the existence of terrace and step sites in the Pt structure will increase its capability for C-C bond activation, which will produce undesired side products. According to the CO-DRIFT data, adding Ge to the catalysts has also decreased the percentage of these high-energy sites, which also has positive effects on enhancing the selectivity.

The intrinsic activity of the samples was further evaluated by determining turnover frequency (TOF) values. For this purpose, reactions were carried out at a lower conversion to ensure kinetic regime, and the related data are presented in Fig. 7. Initial TOF of Pt_2/SiO_2, Pt_2-Ge_2/SiO_2, and Pt_2-Ge_5/SiO_2 are 0.28 1/S, 0.23 1/S and 0.30 1/S, respectively. The Pt_2-Ge_5/SiO_2 sample shows the highest TOF and selectivity among all the catalysts. The TOF of the monometallic Pt_2/SiO_2 is higher than that of the sample with 2 wt% Ge loading. However, the Pt_2/SiO_2 sample exhibited a lower selectivity toward propylene and its deactivation rate was much faster.

Ren et al. reported that upon alloying Pt with Au, an electronic transfer from Pt to Au occurs. In line with this finding, a decrease in TOF during the PDH reaction was observed [16]. Wegener et al. reported an increased TOF for Pt-In catalysts in ethane dehydrogenation.

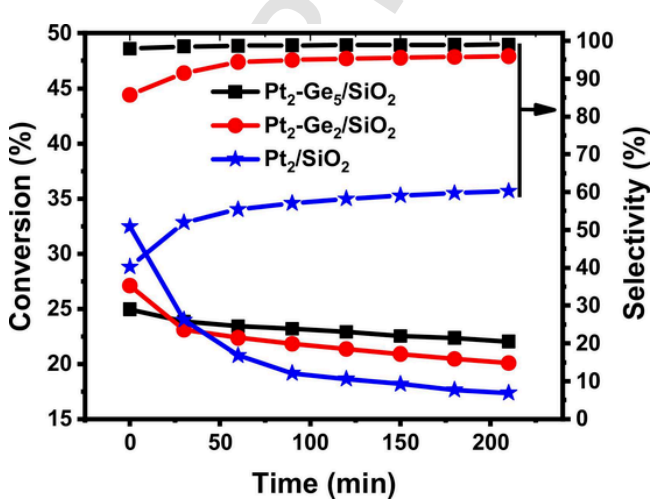

Fig. 6. C_3H_8 conversion and C_3H_6 selectivity of the catalysts (798 K, 5.8 kPa C_3H_8, 5.8 kPa H_2, N_2 used as balance, total flow rate 80 ml/min).

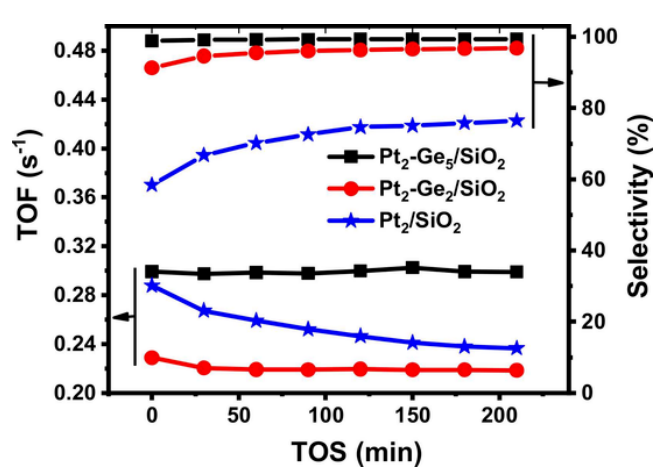

Fig. 7. TOF of the samples with different Ge loading (723 K, 5.8 kPa C_3H_8, 5.8 kPa H_2, N_2 as balance, total flow rate 80 ml/min).

The increase in the TOF was ascribed to an electronic effect (it donates electrons to Pt) and to the faster alkene desorption due to its weaker adsorption on the Pt surface, resulting in faster turnover of active sites [22]. It was also predicted that introduction of Sn into the structure of Pt would lower the desorption barrier of propylene and its derivatives from the surface of Pt to the gas phase. This faster desorption of propylene and its derivatives from the Pt surface would facilitate their diffusion away from the active sites, resulting in an enhancement of the turnover rate of the active sites [12,39].

Upon introducing 2 wt% Ge, the TOF decreased due to the electron-deficient state of Pt, which is in good agreement with the results reported for Pt-Au [16]. However, due to the faster desorption of propylene from the Pt surface, as clearly demonstrated by C_3H_6-TPD results, further increasing the Ge loading results in increasing TOF, which aligns with the prediction of previous works that TOF would increase when there is faster desorption of C_3H_6 from the surface [22,40].

It is important to highlight that our experimental results validate previous theoretical simulations predicting a positive effect of Ge on light alkane dehydrogenation reported by Jimenez-Izal et al. [41]. In this work, it was reported that upon alloying Pt with Ge, the affinity of Pt clusters toward alkenes decreases, enhancing alkenes desorption. Moreover, it was also highlighted that Ge reduces the affinity of the catalyst to carbon, enhancing the coke deactivation resistance of the catalyst. Besides, the authors also predicted that Ge quenches unpaired electrons of Pt, which are needed to activate the alkenes, suppressing side reactions.

Accordingly, a contribution of electronic and geometric effects due to alloy formation facilitates propylene desorption, enhances selectivity, and increases resistance to coke formation.

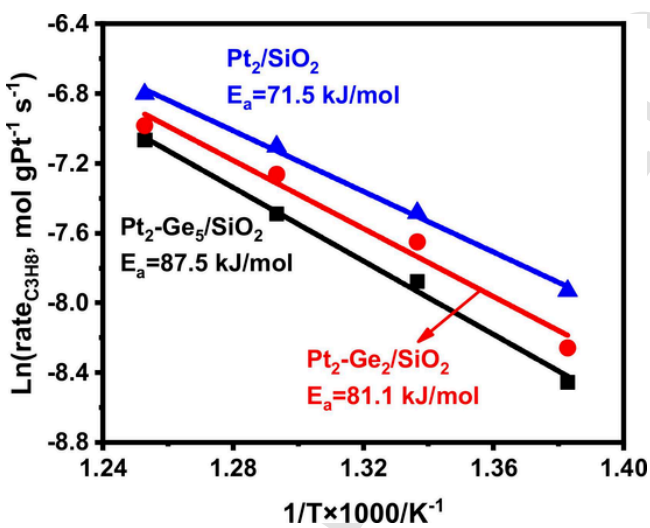

Fig. 8. Arrhenius plots of the samples with different Ge loading (723–798 K, 5.8 kPa C_3H_8, 5.8 kPa H_2, N_2 as balance, total flow rate 80 ml/min).

3.5. Kinetic study

3.5.1. Apparent activation energy

To further explore the effect of Ge addition on the catalytic performance of Pt, apparent activation energies were determined from the Arrhenius plots obtained by performing the PDH reaction at different temperatures and fitting the reaction rate using the Arrhenius law. As depicted in Fig. 8, all the measured activation energies are between 70 kJ/mol and 90 kJ/mol, which are reasonable values according to the reported activation energies for this reaction on different Pt-based catalysts [1,42]. The activation energy for Pt_2/SiO_2 is 71.5 kJ/mol, while it increases to 81.1 kJ/mol and 87.5 kJ/mol with increasing the Ge loading from 2 wt% to 5 wt%, respectively.

Wu et al. reported similar observations for the activation energy for Pd-In bimetallic catalysts during ethane dehydrogenation [43]. They reported that after incorporating In into the Pd structure, the activation energy increased due to changes in the structure and surface properties of Pd. Similarly, Wegener et al. reported that adding In to Pt at increasing In loadings led to an increase in the activation energies for the PDH reaction due to geometric changes in Pt ensembles [22]. Accordingly, the difference in the activation energy of the samples also suggests that upon introducing Ge into the samples, the surface structures changed. This finding is in good agreement with our XAS, XPS, and CO-DRIFTS data depicted in Figs. 2–4, which show that Ge both dilutes Pt surfaces and simultaneously withdraws electrons from Pt due to alloy formation. This alloy formation also decreases the activity of Pt, resulting in an increase in activation energies [28].

These differences in the apparent activation energies of the samples along with differences in the adsorption energies of propylene on the samples (depicted in Fig. 5(b)) may also result in a different reaction mechanism, which needs to be elaborated in detail.

3.5.2. Reaction orders

To determine the reaction orders with respect to H_2 and C_3H_8, a thorough kinetic study was performed using low partial pressures of hydrogen and propane (less than 12 kPa) in the feed flow. Prior to the measurements, it was confirmed that there was no mass transfer or equilibrium limitations under the experiment conditions used for this study (Fig. S9) (propane conversion was kept to less than 10 % for all the samples). In Fig. 9, Ln (TOF) versus Ln(P) plots are depicted to de-

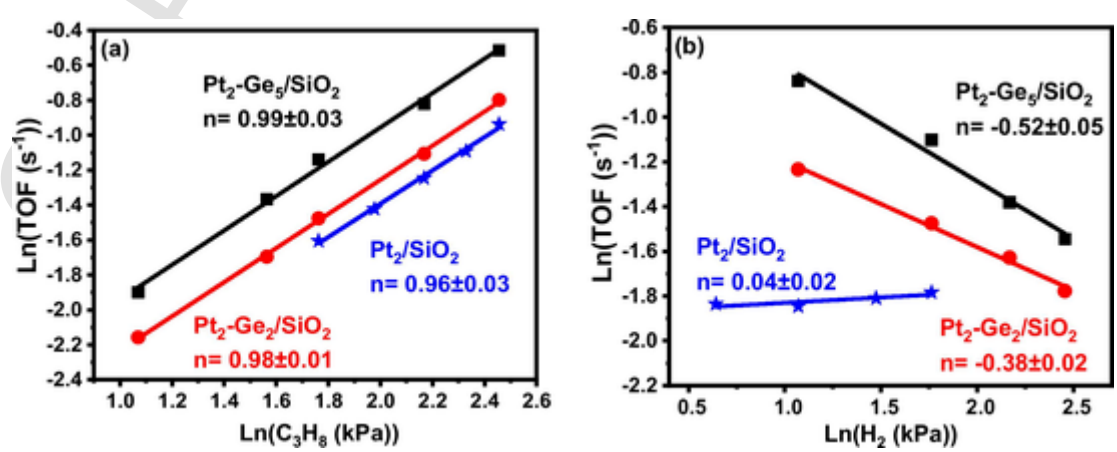

Fig. 9. TOFs of the samples as a function of partial pressures: (a) propane and (b) hydrogen (723 K, 2–12 kPa C_3H_8, 1–10 kPa H_2, N_2 as balance and a total flow rate of 80 ml/min).

termine the apparent reaction orders. According to these kinetic data, the reaction order of C_3H_8 remains close to 1 regardless of Ge loading (Fig. 9. (a)), while the reaction order of H_2 strongly depends on the Ge loading (Fig. 9. (b)). For Pt_2/SiO_2, the reaction order of H_2 is almost 0, while it decreases to − 0.38 when the Ge loading is 2 wt%. An additional increase in the Ge loading to 5 wt%, further decreases the reaction order to − 0.52.

Cortright et al. reported a negative reaction order with respect to hydrogen and a first reaction order to isobutane in isobutane dehydrogenation [44]. The negative reaction order with respect to hydrogen was attributed to the competitive adsorption of hydrogen on the metal sites, which blocks the sites required for the adsorption of isobutane. Accordingly, the changes in the hydrogen order were attributed to variations in the hydrogen coverage on the surface. On the other hand, the first reaction order rate with respect to isobutane was related to a very low surface coverage by adsorbed isobutyl species. Since the kinetic study was carried out at low conversion and low isobutane partial pressure, this constant first-order reaction rate was expected. In good agreement with Cortright et al.'s results, Virnovskaia et al. also reported a first-order reaction rate (~0.95) with respect to ethane and a negative reaction order for hydrogen during ethane dehydrogenation reaction [45]. The negative reaction order for hydrogen was ascribed to the competitive coverage of active surface sites by a stronger hydrogen adsorption [46]. Therefore, a negative reaction order of hydrogen for the Ge-promoted catalysts (see Fig. 9) is the result of the modification of the adsorption properties of the Pt surface by Ge. The changes induced by the presence of the Ge species, boosting the hydrogen adsorption capacity of the catalyst, increase the metallic coverage by hydrogen and consequently decrease the values of the observable kinetic orders [46]. On the other hand, since the reactions were carried out at a low conversion and low partial pressure of propane, a constant first reaction order is reasonable and in good agreement with the similar studies on light alkane dehydrogenation [44,45]. These results will be further investigated in the next section.

3.5.3. Insights into the reaction mechanism

Following the Langmuir-Hinshelwood-Hougen-Watson (LHHW) formalism [47], we have considered two plausible reaction mechanisms for explaining the kinetics results presented in Figs. 8 and 9.

The first mechanism considered was proposed by Zhu et al. [25] for the prediction of the reaction rate of Pt nanoparticles of different cluster sizes in the PDH reaction and is described by the following elemental reactions: (i) propane adsorption; (ii) first C-H bond cleavage; (iii) second C-H bond cleavage; (iv) propylene desorption; and (v) hydrogen desorption [48,49]:

i) $C_3H_8 + L \overset{k_1,k_{-1}}{\longleftrightarrow} C_3H_8L$
$K_1 = k_1/k_{-1} = \theta_{C_3H_8L}/P_{C_3H_8}\theta_L$

ii) $C_3H_8L + L \overset{k_2,k_{-2}}{\longleftrightarrow} C_3H_7L + HL$
$K_2 = k_2/k_{-2} = \theta_{C_3H_7L}\theta_{HL}/\left(\theta_{C_3H_8L}\theta_L\right)$

iii) $C_3H_7L + L \overset{k_3,k_{-3}}{\longleftrightarrow} C_3H_6L + HL$
$K_3 = k_3/k_{-3} = \theta_{C_3H_6L}\theta_{HL}/\left(\theta_{C_3H_7L}\theta_L\right)$

iv) $C_3H_6L \overset{k_3,k_{-3}}{\longleftrightarrow} C_3H_6 + L$
$K_4 = k_4/k_{-4} = 1/K_{C_3H_6} = P_{C_3H_6}\theta_L/\theta_{C_3H_6L}$

v) $2HL \overset{k_4,k_{-4}}{\longleftrightarrow} H_2 + 2L$
$K_5 = k_5/k_{-5} = 1/K_{H_2} = P_{H_2}\theta_L^2/\theta_{HL}^2$

For this mechanism with five steps, we have considered three cases depending on the assumed "rate determinant step" (rds). Thus, in Case A-1, the rds is the adsorption of propane; in Case A-2, the rds is the first C-H bond cleavage; and in Case A-3, the rds is the second C-H bond cleavage. In all the cases, the rest of the steps are considered to be in equilibrium [25,47].

The second mechanism considered assumes that propane adsorption is dissociative, with the rest of the steps being the same as in the first mechanism. Thus, the reaction network is:

i) $C_3H_8 + 2L \overset{k_1,k_{-1}}{\longleftrightarrow} C_3H_7L + HL \quad ; \quad K_1 = k_1/k_{-1}$

ii) $C_3H_7L + L \overset{k_2,k_{-2}}{\longleftrightarrow} C_3H_6L + HL \quad ; \quad K_2 = k_2/k_{-2}$

iii) $C_3H_6L \overset{k_3,k_{-3}}{\longleftrightarrow} C_3H_6 + L \quad ; \quad K_3 = k_3/k_{-3} = 1/K_{C_3H_6}$

iv) $2HL \overset{k_4,k_{-4}}{\longleftrightarrow} H_2 + 2L \quad ; \quad K_4 = k_4/k_{-4} = 1/K_{H_2}$

For this second mechanism, we have considered two cases. In Case B-1, the rds is the dissociative adsorption of propane over two active sites; and in Case B-2, the rds is the second C-H bond cleavage (step ii). In both cases, the rest of the steps are considered in equilibrium [25, 47]. In addition to the kinetic expressions for each case, we have also derived the relationship between the apparent kinetic orders with respect to hydrogen and the hydrogen surface coverage. Table 3 summarizes all these equations and the detailed derivation of all kinetic equations, and the non-linear regression calculations following the LHHW formalism are reported in Supplementary Information.

Tables S13–S16 summarize all fitting results along with the statistical parameters. From the statistics point of view, several models could be adopted for both monometallic and Ge-promoted catalysts, namely Case A-1, A-2, and B-1. However, the kinetic parameters derived from the last two cases seem more meaningful. Thus, our kinetic analysis suggests the rds is either the first C-H cleavage in the first mechanism, Case A-2, or the dissociative adsorption of propane over two active sites in the second one, Case B-1. In addition, it is clear the models based on the second C-H cleavage, Cases A-3 and B-3, cannot satisfactorily describe the experimental data of the Pt/SiO_2 catalyst, while significantly better fittings are certainly obtained for the Ge-promoted sample, mostly when dissociative propane adsorption is considered as the first step. In the conditions used in this study, the final equations for Cases A-1 and B-1, (see Table S12), are the same, making the two cases indistinguishable. For the sake of simplicity, Case A-2 is adopted. Table 4 summarizes the kinetic parameters derived from the fitting of the experimental data for Case A-2, along with the statistical parameters reported in Table S14.

Simulations using an extensive reaction network on Pt(111) showed that increasing the H_2/C_3H_8 ratio in the feed up to 3 increases the site time yield (STY) of propylene, reaching a maximum. However, no further increase in the STY is predicted at higher H_2/C_3H_8 ratios [50]. On the other hand, using DFT simulations, it was reported that the rate of propylene production first increases then declines as the H_2/C_3H_8 ratio is increased, reaching a maximum at a H_2/C_3H_8 ratio of 1.33. This maxi-

Table 3
Summary of reaction rates and hydrogen orders.

Case	Reaction rate	Hydrogen kinetic order (n)
A-1	$(-r_{C_3H_8}) = \frac{k_1 P_{C_3H_8}}{\left(1+\sqrt{K_{H_2}P_{H_2}}\right)}$	$n = -\frac{\theta_{HL}}{2}$ $-\frac{1}{2}<n<0$
A-2	$(-r_{C_3H_8}) = \frac{k_2 K_1 P_{C_3H_8}}{\left(1+\sqrt{K_{H_2}P_{H_2}}+K_1 P_{C_3H_8}\right)^2}$	$n = -\theta_{HL}$ $-1<n<0$
A-3	$(-r_{C_3H_8}) = \frac{k_3 K_1 K_2 P_{C_3H_8}}{\sqrt{K_{H_2}P_{H_2}}\left(1+\sqrt{K_{H_2}P_{H_2}}+K_1 P_{C_3H_8}\cdot\left(1+\frac{K_2}{\sqrt{K_{H_2}P_{H_2}}}\right)\right)^2}$	$n = -\theta_{HL} - \frac{1}{2}$ $-\frac{3}{2}<n<-\frac{1}{2}$
B-1	$(-r_{C_3H_8}) \cong \frac{k_1 P_{C_3H_8}}{\left(1+\sqrt{K_{H_2}P_{H_2}}\right)^2}$	$n = -\theta_{HL}$ $-1<n<0$
B-2	$(-r_{C_3H_8}) = \frac{k_2 K_1 P_{C_3H_8}}{\sqrt{K_{H_2}P_{H_2}}\left(1+\sqrt{K_{H_2}P_{H_2}}+\frac{K_1 P_{C_3H_8}}{\sqrt{K_{H_2}P_{H_2}}}\right)^2}$	$n = -\theta_{HL} - \frac{1}{2}$ $-\frac{3}{2}<n<-\frac{1}{2}$

CORRECTED PROOF

Table 4
Summary of the kinetic parameters for Case A-2 derived from the fittings of experimental data.

	Pt_2/SiO_2		Pt_2-Ge_2/SiO_2		Pt_2-Ge_5/SiO_2	
	Value	*Conf. Interv.*	*Value*	*Conf. Interv.*	*Value*	*Conf. Interv.*
k_{obs}	0.0319	± 0.0020	0.01059	± 0.0219	0.2512	± 0.0950
K_{H2}	0	–	0.0709	± 0.0360	0.2090	± 0.1477
K_1	0	–	0.0015	± 0.0056	0.0101	± 0.0117

mum occurs when the negative effect of four-fold hollow sites overtakes the positive effect of free step sites [51].

Indeed, a beneficial H_2 effect has been observed in the Pt-Ge bimetallic samples used in this work, which is manifested by the increased selectivity toward propylene and the dressed coke deposition as compared to in the monometallic sample. This beneficial effect can be certainly attributed to a reduced coverage of deep dehydrogenated species, along with the gasification of coke deposited on the surface of the Ge-promoted samples, in good agreement with a previous work [50]. Moreover, our C_3H_6-TPD and C_3H_8-TPD data show that upon introducing Ge, both propane and propylene desorb faster. Thus, stronger adsorption of C_3H_8 on the monometallic Pt sample results in a higher conversion, particularly at the beginning of the reaction when the catalyst has not been yet deactivated by coke formation [38]. On the other hand, stronger adsorption of C_3H_6 on this sample allows for side reactions to take place, resulting in lower selectivity. Accordingly, the better catalytic performance of the bimetallic samples is also due to the interaction of Pt and Ge, which modifies the adsorption energy of reactants and products at the active sites.

Considering the results from the LHHW analysis, along with the experimental values of the reaction orders for propane and hydrogen obtained for the Pt_2/SiO_2 catalyst (1.10 ± 0.17 and 0.165 ± 0.173 respectively), the first C-H bond cleavage is most likely the rate-determining step for the monometallic sample. However, while the reaction order for propane remains close to 1, for the bimetallic samples (0.997 ± 0.120 for Pt_2-Ge_2/SiO_2 and 0.943 ± 0.207 for Pt_2-Ge_5/SiO_2), the reaction order with respect to H_2 is negative and close to − 0.5 for both samples (−0.379 ± 0.135 and −0.495 ± 0.225, respectively). As shown by the LHHW modelling (see Table 4), higher hydrogen adsorption constants are obtained for both bimetallic catalysts. This fact, along with the decrease in the adsorption strength of propylene clearly shown by the C_3H_6-TPD profiles, can satisfactorily explain the enhanced propylene selectivity and the change of the apparent activation energy as experimentally observed. However, a changed in the reaction mechanism for the bimetallic samples cannot be completely ruled out.

4. Conclusion

In this study, catalyst characterizations and kinetic analysis were combined to study catalytic performance of Ge-modified Pt nanoparticles supported on SiO_2 during propane dehydrogenation. A neutral SiO_2 support with a high surface area was utilized to rule out the support effect, allowing for the establishment of a univocal structural/electronic property-catalytic performance relationship and the impact of Pt-Ge alloy on the reaction mechanism. The interaction between Pt and Ge modifies the geometric and electronic properties of Pt due to alloy formation. The Pt-Ge alloy lowers the adsorption energy of propylene on the Pt surface and decreases the activity for C-C bond cleavage, resulting in a lower coke formation rate and higher selectivity.

A detailed kinetic study reveals that the reaction order with respect to propane remains close to 1 for all samples used in this work (i.e., Pt_2/SiO_2, Pt_2-Ge_2/SiO_2, and Pt_2-Ge_5/SiO_2), while the reaction order with respect to H_2 varies between 0 and − 0.5. The negative reaction order with respect to H_2 is due to the blockage of the active metal surface by hydrogen. In addition, the kinetic analysis indicates that the first C—H bond cleavage is most likely the rate-determining step and the addition of Ge strengthens the hydrogen adsorption of the Ge samples.

CRediT authorship contribution statement

Sajjad Rimaz designed the research plan, performed the catalyst synthesis, most of catalyst characterization and testing and drafted the manuscript; Mohammadreza Kosari performed TEM analysis and additional experiments; Chen Luwei supervised analysis and discussion of experimental results; Xi Shibo carried out XAS experiments and analysis; Antonio Monzón performed kinetic modelling; Sibudjing Kawi and Armando Borgna were was responsible for the overall direction of the project and the final manuscript.

Declaration of Competing Interest

The authors declare that they have no known competing financial interests or personal relationships that could have appeared to influence the work reported in this paper.

Acknowledgements

The authors gratefully acknowledge the financial support by the Agency for Science, Technology and Research (A*STAR) of Singapore (AME-IRG Grant No. A1783c0016), and the National University of Singapore. Sajjad Rimaz is tankful to A*STAR for the Singapore International Graduate Award (SINGA) scholarship. We thank the assistance of Ms Wang Zhan April for XPS measurements.

Conflict of interests

There are no conflicts to declare.

Appendix A. Supporting information

Supplementary data associated with this article can be found in the online version at doi:10.1016/j.apcata.2022.118751.

References

[1] H.Z. Wang, W. Zhang, J.W. Jiang, Z.J. Sui, Y.A. Zhu, G.H. Ye, D. Chen, X.G. Zhou, W.K. Yuan, Catal. Sci. Technol. 9 (2019) 867–876.
[2] E.J. Jang, J. Lee, H.Y. Jeong, J.H. Kwak, Appl. Catal. A: Gen. 572 (2019) 1–8.
[3] S. Rimaz, R. Halladj, S. Askari, J. Colloid Interface Sci. 464 (2016) 137–146.
[4] B. Li, Z. Xu, F. Jing, S. Luo, W. Chu, Appl. Catal. A: Gen. 533 (2017) 17–27.
[5] Y. Zhu, Z. An, H. Song, X. Xiang, W. Yan, J. He, ACS Catal. 7 (2017) 6973–6978.
[6] N. Dewangan, A. Jangam, M. Sethia, S. Das, S. Pati, H. Kus, S. Kawi, ChemCatChem 11 (2019) 4923–4934.
[7] K. Searles, K.W. Chan, J.A. Mendes Burak, D. Zemlyanov, O. Safonova, C. Copéret, J. Am. Chem. Soc. 140 (2018) 11674–11679.
[8] N. Kaylor, R.J. Davis, J. Catal. 367 (2018) 181–193.
[9] G. Liu, L. Zeng, Z.J. Zhao, H. Tian, T. Wu, J. Gong, ACS Catal. 6 (2016) 2158–2162.
[10] J. Im, M. Choi, ACS Catal. 6 (2016) 2819–2826.
[11] F. Jiang, L. Zeng, S. Li, G. Liu, S. Wang, J. Gong, ACS Catal. 5 (2014) 438–447.
[12] L. Nykänen, K. Honkala, ACS Catal. 3 (2013) 3026–3030.
[13] M. Sheintuch, O. Liron, A. Ricca, V. Palma, Appl. Catal. A: Gen. 516 (2016) 17–29.
[14] S. Tan, L.B. Gil, N. Subramanian, D.S. Sholl, S. Nair, C.W. Jones, J.S. Moore, Y. Liu, R.S. Dixit, J.G. Pendergast, Appl. Catal. A: Gen. 498 (2015) 167–175.
[15] J.J. Sattler, J. Ruiz-Martinez, E. Santillan-Jimenez, B.M. Weckhuysen, Chem. Rev. 114 (2014) 10613–10653.
[16] G.Q. Ren, G.X. Pei, Y.J. Ren, K.P. Liu, Z.Q. Chen, J.Y. Yang, Y. Su, X.Y. Liu, W.Z. Li, T. Zhang, J. Catal. 366 (2018) 115–126.
[17] E. Jimenez-Izal, H. Zhai, J.-Y. Liu, A.N. Alexandrova, ACS Catal. 8 (2018) 8346–8356.
[18] L. Gonçalves Cesar, C. Yang, Z. Lu, Y. Ren, G. Zhang, J.T. Miller, ACS Catal. (2019).
[19] J.Z. Chen, Z. Wu, X. Zhang, S. Choi, Y. Xiao, A. Varma, W. Liu, G. Zhang, J.T. Miller, Catal. Sci. Technol. 9 (2019) 1349–1356.
[20] C. Ye, Z. Wu, W. Liu, Y. Ren, G. Zhang, J.T. Miller, Chem. Mater. 30 (2018) 4503–4507.
[21] Z. Wu, B.C. Bukowski, Z. Li, C. Milligan, L. Zhou, T. Ma, Y. Wu, Y. Ren, F.H.

CORRECTED PROOF

Ribeiro, W.N. Delgass, J. Am. Chem. Soc. 140 (2018) 14870–14877.
[22] E.C. Wegener, Z. Wu, H.T. Tseng, J.R. Gallagher, Y. Ren, R.E. Diaz, F.H. Ribeiro, J.T. Miller, Catal. Today 299 (2018) 146–153.
[23] A. Virnovskaia, E. Rytter, U.J.I. Olsbye, E.C. Research, Ind. Eng. Chem. Res. 47 (2008) 7167–7177.
[24] G. Siddiqi, P. Sun, V. Galvita, A.T. Bell, J. Catal. 274 (2010) 200–206.
[25] J. Zhu, M.L. Yang, Y. Yu, Y.A. Zhu, Z.J. Sui, X.G. Zhou, A. Holmen, D. Chen, ACS Catal. 5 (2015) 6310–6319.
[26] S. Rimaz, L. Chen, S. Kawi, A. Borgna, Appl. Catal. A: Gen. (2019) 117266.
[27] Z. Han, S. Li, F. Jiang, T. Wang, X. Ma, J. Gong, Nanoscale 6 (2014) 10000–10008.
[28] S. Rimaz, L. Chen, A. Monzón, S. Kawi, A. Borgna, Chem. Eng. J. 405 (2020) 126656.
[29] S. Rimaz, M. Kosari, L. Chen, S. Kawi, A. Borgna, Mol. Catal. 510 (2021) 111672.
[30] R.Z. Lei, A.J. Gellman, B.E. Koel, Surf. Sci. 554 (2004) 125–140.
[31] Y. Du, Y. Zhu, S. Xi, P. Yang, H.O. Moser, M.B. Breese, A. Borgna, J. Synchrotron Radiat. 22 (2015) 839–843.
[32] B. Zhang, L. Zheng, Z. Zhai, G. Li, G. Liu, ACS Appl. Mater. Interfaces (2021).
[33] M. Alvarez-Galvan, R. Navarro, F. Rosa, Y. Briceño, F.G. Alvarez, J. Fierro, Int. J. Hydrog. Energy 33 (2008) 652–663.
[34] L.L. Long, W.Z. Lang, X. Yan, K. Xia, Y.J. Guo, Fuel Process. Technol. 146 (2016) 48–55.
[35] T. Garetto, A. Borgna, C. Apesteguia, Stud. Surf. Sci. Catal. 101 (1996) 1155–1164.
[36] G. Sun, Z.J. Zhao, R. Mu, S. Zha, L. Li, S. Chen, K. Zang, J. Luo, Z. Li, S. Purdy, Nat. Commun. 9 (2018) 4454.
[37] A. Borgna, T. Garetto, C. Apesteguıa, B. Moraweck, Appl. Catal. A: Gen. 182 (1999) 189–197.
[38] L. Sun, Y. Chai, W. Dai, G. Wu, N. Guan, L. Li, Catal. Sci. Technol. 8 (2018) 3044–3051.
[39] M.L. Yang, Y.A. Zhu, X.G. Zhou, Z.J. Sui, D. Chen, ACS Catal. 2 (2012) 1247–1258.
[40] C. Yang, Z. Wu, G. Zhang, H. Sheng, J. Tian, Z. Duan, H. Sohn, A.J. Kropf, T. Wu, T.R. Krause, Catal. Today 323 (2019) 123–128.
[41] E. Jimenez-Izal, J.Y. Liu, A. Alexandrova, J. Catal. 374 (2019) 93–100.
[42] Y. Shan, Z. Sui, Y. Zhu, D. Chen, X. Zhou, Chem. Eng. J. 278 (2015) 240–248.
[43] Z. Wu, E.C. Wegener, H.T. Tseng, J.R. Gallagher, J.W. Harris, R.E. Diaz, Y. Ren, F.H. Ribeiro, J.T. Miller, Catal. Sci. Technol. 6 (2016) 6965–6976.
[44] R.D. Cortright, P.E. Levin, J.A. Dumesic, Ind. Eng. Chem. Res. 37 (1998) 1717–1723.
[45] A. Virnovskaia, E. Rytter, U. Olsbye, Ind. Eng. Chem. Res. 47 (2008) 7167–7177.
[46] S. Armenise, E. García-Bordejé, J.L. Valverde, E. Romeo, A. Monzón, Phys. Chem. Chem. Phys. 15 (2013) 12104–12117.
[47] M.A. Vannice, Kinetics of Catalytic Reactions, Chapter 7, Springer, New York (USA), 2005.
[48] Q. Li, Z. Sui, X. Zhou, D. Chen, Appl. Catal. A: Gen. 398 (2011) 18–26.
[49] S. Gómez-Quero, T. Tsoufis, P. Rudolf, M. Makkee, F. Kapteijn, G. Rothenberg, Catal. Sci. Technol. 3 (2013) 962–971.
[50] S. Saerens, M.K. Sabbe, V.V. Galvita, E.A. Redekop, M.-Fo Reyniers, G.B. Marin, ACS Catal. 7 (2017) 7495–7508.
[51] L. Xiao, Y.L. Shan, Z.J. Sui, D. Chen, X.G. Zhou, W.K. Yuan, Y.A. Zhu, ACS Catal. 10 (10) (2020) 14887–14902.

CORRECTED PROOF